Version of Record: https://www.sciencedirect.com/science/article/pii/S0924013623001061
Manuscript_407752440514077b094644ca78815931

Effects of printed bead volume on thermal history, polymer degree of crystallinity and mechanical properties in large scale additive manufacturing.

L. Malagutti[1], S. Charlon[2*], V. Mazzanti[1], F. Mollica[1]

1. Department of Engineering, Università degli Studi di Ferrara, via Saragat 1, Ferrara 44122, Italy

2. IMT Nord Europe, Institut Mines-Télécom, Univ. Lille, Centre for Materials and Processes, Cité scientifique, rue Guglielmo Marconi, BP 20145, F-59653 Villeneuve d'Ascq Cedex, France

[*] corresponding author: sebastien.charlon@imt-nord-europe.fr

Abstract:

One of the promising innovations in additive manufacturing by material extrusion is the usage of large machines that allow building big parts in shorter times. In this case, though, the complex interactions between materials and processing (polymer plasticization, polymer chains inter-diffusion, inter-bead fusion, polymer crystallization etc.) are still not completely understood. The present work brings novel fundamental and quantitative knowledge that would contribute to the development of this technology. Specimens made of a semicrystalline polylactic acid were printed using different bead volumes with a single screw extruder mounted on a robot arm. A cascade effect was identified during production runs: variations in the bead volumes substantially impacted the thermal histories, which influenced polymer crystallization, and this in turn affected the mechanical properties. As a result, a substantial heterogeneity in the degree of crystallinity could be generated in large 3D printed parts, that would induce locally different mechanical properties. Thus, it is clear that not only inter-bead junctions must be considered for understanding the mechanical properties,

but also the extent of crystallization of the polymer. Finally, thermal histories of the beads were precisely measured, and these valuable data could help the scientific community to better understand the evolutions of the bead temperature during the production runs.

Keywords: pellet extruder, Fused Filament Fabrication; Fused Deposition Modeling, nozzle diameter; bead volume, cooling kinetics.

1 Introduction

Among the various additive manufacturing (AM) technologies, material extrusion 3D printing, commonly named fused filament fabrication (FFF), is very popular because of its easiness to shape many thermoplastic polymers into complex and personalized parts, as described by Bayart et al. (2021). Objects are produced through a layer-by-layer deposition of a molten thermoplastic material, each layer being obtained by extruding single beads one after the other one, following a certain path.

The starting point of FFF is a CAD model of the part to be produced (typically in STL format). Next, a suitable slicing software is used to create a file named “G-code”, which contains the numerous printing instructions that would be read and executed by the 3D printer to build the part, such as the extruder path, the processing temperatures, the width and height of the beads, etc. Mazzanti et al. (2019) grouped such parameters into three main categories, i.e. those linked to extruder geometry, to processing and the structural ones.

Although additive manufacturing, and FFF in particular, was born to produce mainly prototypes of limited size, it is gaining more and more market shares for small scale production and even for bigger parts as described by Shaik et al. (2021). Cleeman et al. (2022) summarized the different

technologies to make these parts by material extrusion in a relatively low production time and described their advantages and disadvantages with great detail. Briefly, these technologies are based on of the use of:

(i) two nozzles of different diameters allowing to rapidly print low-resolution features and to slowly print only high-resolution features;

(ii) several printing heads to print different sections of the same part simultaneously. Several configurations were developed: all printing heads can be mounted on only one gantry or on independent gantries and several co-robot arms or mobile robots can be used;

(iii) a large nozzle diameter. In this case, common FFF printing head fed with filaments and equipped with a large nozzle diameter or an extruder fed with pellet materials mounted on a gantry or a robot can be used.

Gupta at al. (2021) reported that the last-mentioned technology allows high polymer flow rates and this in turn reduces the printing time of large parts. Moreover, pellets are cheaper than filaments and offer a greater versatility in terms of available materials. On the other hand, Kristiawan et al. (2021) highlighted the difficulties to respect tolerances with larger nozzles.

When printing structural parts, though, one of the main problems is that the mechanical properties are lower than those of objects obtained by traditional manufacturing techniques, such as injection molding (Behzadnasab et al., 2017), with the possible exception of impact strength as described by Wang et al. (2017). Habeeb et al. (2016) explained these results by the presence of voids, while Li et al. (2018) pointed out to the poor quality of the welds between the subsequently deposed beads and layers.

Several approaches were described in the literature to optimize the mechanical properties of 3D printed parts. Costa et al. (2017) demonstrated the possibility to modulate this weld quality by controlling the temperature of the printed beads. Jin et al. (2017) reported an increase in the

elongation at break in about 50% of parts printed in PLA using a chemical post-treatment and Malagutti et al. (2022a) studied a remelting and compaction treatment that led to void reduction and better interlayer welding. In the scientific literature there is a remarkable number of papers dealing with the optimization of printing parameters to maximize the mechanical properties. Since the number of printing parameters is quite high, a design of experiments approach is commonly followed. It was found that the main parameters influencing the mechanical properties are the infill percentage, the raster angle (Malagutti et al., 2022b), the build orientation and the air gap (Sooda et al., 2010). All of these papers considered only the case of traditional filament fed extruders, characterized by small diameter nozzles (0.4 – 1.0 mm). In this case, Kuznetsov et al. (2018) found that mechanical properties increased with the nozzle size, both in tension and bending and this can be easily justified by the smaller number of deposited beads in a layer, which in turn decreases the number of intralayer bonds.

The case of larger nozzles has been considered very little so far. It has some peculiar differences with respect to filament extruders, which come from the greater heat capacity of the deposited beads. This implies that, under the same printing conditions, cooling rate will be slower, thus temperature would remain high over a longer time. However, like in FFF, a non-trivial thermal history is generated due to the extruder path, that consists in a succession of heating and cooling steps, and this would depend also on the particular location within the part. For example, the central portion of a part remains hotter for a longer time if compared to the external surface that is in direct contact with air. Because of the greater heat capacity of big beads, the thermal heterogeneities are substantially different between parts produced by conventional FFF and by a large-scale AM machine.

Alsoufi et al. (2017) indicated that amorphous thermoplastics are normally preferable for FFF over semi-crystalline ones, because of the easier deposition process, lower shrinkage, and warpage effects. Moreover, in the case of semicrystalline materials variations in thermal conditions of the

deposed layers reflect themselves into important differences in the mechanical properties of the finished product. In fact, Liao et al. (2019) showed that the crystalline structure of the polymer is highly dependent on thermal history and Northcuttsara et al. (2018) indicated that the extent to which crystallization occurs is a function of process characteristic temperatures and times. Vodari et al. (2013) proved that the consequent differences in crystallinity have a direct influence on the mechanical properties of the printed material.

To the best of the authors' knowledge, no study was yet performed to clearly understand the direct consequences of large bead volumes on material thermal history as a function of their location in the part, on the microstructure of the polymer and therefore on the resulting mechanical properties. The present paper aims at this missing knowledge. A semi-crystalline poly-(L-lactic acid), or PLLA, commonly used in FFF, was employed as a model material, like in the work of Wasanasuk et al. (2011), to highlight the different mechanical properties that can be induced by crystallinity through the process related thermal history. First, samples made with several bead volumes were produced with a self-assembled large 3D printer equipped with various nozzle diameters (between 3 to 8 mm) (Fig.1), allowing to modulate the bead size constituting each printed sample. During the production run, the thermal histories of deposited beads were recorded at 3 locations of interest. The impacts of these thermal histories on the microstructures of the PLLA were then studied by differential scanning calorimetry. Finally, flexural mechanical properties were measured, because bending loads are often dangerous for structural integrity of parts, and then correlated to the thermal history and crystallinity.

Fig. 1. Picture of the self-assembled large 3D printer used in the study.

2 Experimental methods

2.1 Material

The PLA used in this work was a poly-(L-lactic acid) and was purchased from Natureplast (France) named PLE 005, which features a density of 1.25 g/cm^3, a melt flow index of 7 g/10min (190°C, 2.16 kg) and a melting temperature of 155°C, according to the technical data sheet of the material. Before printing, the pellets were dried at 55°C for 24 hours in a drier (FASTI KOCH ERD Xpert+, Koch Technik) and the material was fed directly from the drier to the extruder through a compressor to avoid hydrolysis.

2.2 Part preparation

2.2.1 Compression molding

As a reference for the mechanical properties of the material, ISO 178 standard specimens (80 mm x 10 mm x 4 mm) were compression molded, like in the work of Forster et al. (2015), using a Dolouets 383 thermo-moulding press (France). After drying the pellets in an oven at 55°C for 24 h, the pellets were heated for 10 minutes at 200°C under atmospheric pressure in the mold and then a 150 bar pressure was applied for 5 minutes at the same temperature. Completely amorphous parts were obtained by quenching the material in water right after compression molding, while a slow cooling rate (i.e. less than 1°C/min) was applied to obtain highly crystalline parts. In both cases, parts were held in the mold before demolding to maintain dimensional tolerances.

2.2.2 Material extrusion

Specimens were obtained using a self-assembled 3D printing platform, called "LASCALA", patented by Dorez et a. (2019). This platform is equipped with a pellet fed single screw extruder mounted on a Stäubli TX200 robot arm, itself mounted on a 7 m length ALSS-1R rail supplied from Lucas (France), allowing to achieve a build volume of 2 m x 5 m x 1 m, in x, y and z respectively. The extruder barrel, specifically designed by ZeroD (France), has a diameter of 22 mm, length over diameter ratio of 11 and it allows to mount nozzles of various diameters. The maximum screw velocity is 250 RPM and the maximum throughput is around 4 kg/h.

For each nozzle diameter (3 mm, 5 mm, and 8 mm), the molten polymer throughput was adjusted to print the parts with four different bead widths, namely 100%, 125%, 175% and 250% of the nozzle diameter (Tab. 1). This methodology allowed to make large ranges of bead widths per nozzle with cross-over ranges between the various nozzles. For example, bead widths between 8 and 12 mm could be produced both with a 5 mm as well as an 8 mm nozzle diameter. Thus, the influence of the bead volume could be evaluated independently of the nozzle diameter.

Concerning sample dimensions, ISO 178 was followed but the size was scaled up by a factor of 4 in the 3 dimensions, thus with a cross section of approximately 40 x 16 mm and a length of 320 mm.

The part width was chosen in such a way to accommodate at least two beads per layer in the case of the largest bead width, that is 250% of the 8 mm nozzle, i.e. 20 mm.

In order to verify the correspondence with the reference width and to quantify the layer thickness, the effective bead width was measured in the following way. For each printing condition, three different parts that were one bead wide and four layers thick were printed as a test. Next, these 3D printed parts were measured with a digital centesimal caliper to measure the width of a bead and the thickness of a layer. On the basis of these measurements, the number of beads per layer and the number of layers to get the desired cross section could be easily obtained. This information is reported in Tab. 1.

No slicing software was used in this paper: the G-code was written directly using a MATLAB script. The input parameters that had to be specified were the measured bead width and height, the number of beads per layer and the total number of layers. Some of the processing parameters were constant for all parts, i.e. overlap, printing speed and travel speed, and these were equal to 0.3 mm, 20 mm/s and 100 mm/s, respectively. The extruder path was also an important input of the G-code file. This is pictured in Fig. 2: after complete deposition in the longitudinal direction of a single bead, the nozzle was led onto two brushes to clean it and remove the small beads coming from stringing. The deposition continued just beside the bead that was previously deposed in an analogous way until the layer was completed and so on for all the layers. Such a procedure ensured a similar deposition time between two consecutive beads in the same layer, independent of the position, considering that the variations in the oblique nozzle displacements between the bead deposition and the brushes are negligible. The time was estimated to be 41 ± 1 s, since travel and print speed were selected as 100 mm/s and 20 mm/s, respectively. This was important, because it made thermal history of the deposed beads independent of the extruder path. Of course, though, thermal history depended on the location within the cross section of the parts.

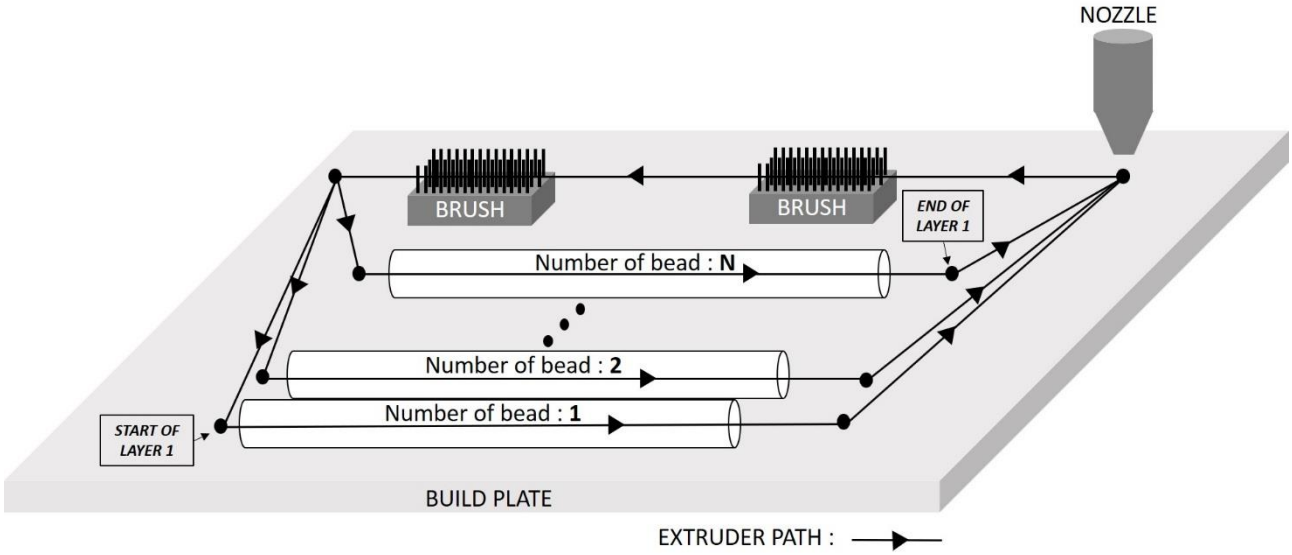

Fig. 2. Schematic representation of the printing path used to build each layer.

Further printing parameters were the processing temperatures. The temperature profile of the extruder was set according to the technical datasheet of the used PLA. In particular, the three zones of the extruder were fixed at 220, 185 and 190°C, from the feeding zone to the die, respectively. Lastly, the screw speed depended on the particular bead width that was printed. These are listed in Tab. 1.

Table 1. Geometric parameters for each printing condition.

Nozzle diameter (mm)	**Set bead width (mm)**	**Number of beads per layer**	**Number of layers**	**Screw speed (RPM)**
3	3	15	15	6
	3.75	11	13	9
	5.25	8	12	15
	7.5	6	11	22
5	5	8	11	16
	6.25	7	11	19
	8.75	5	10	29
	12.5	3	7	61
8	8	5	8	33
	10	4	8	40
	14	3	6	73
	20	2	5	134

2.3 Temperature measurement

Type K thermocouples purchased from TC Direct were used to measure the thermal histories of the 3D printed parts. These sensors had a diameter of 80 µm allowing to minimize the measurement errors due to heat transfer between the sensor and the bead. Temperatures were acquired through a National Instrument data acquisition card (NI 9213) combined to a LabView-based acquisition software. Before each acquisition, the thermocouples were calibrated using a Mettler Toledo FP 80 oven.

The thermal history of beads was measured from deposition down to room temperature in the cross-section located in the middle of each part, i.e. at 160 mm from both ends. Within this cross section, measurement was performed at three different locations, pictured in Fig. 3 as T1, T2 and T3. The T1 and T2 thermocouples were placed on the build plate to record the temperatures of the first layer, while the T3 thermocouple acquired the temperature of the part center.

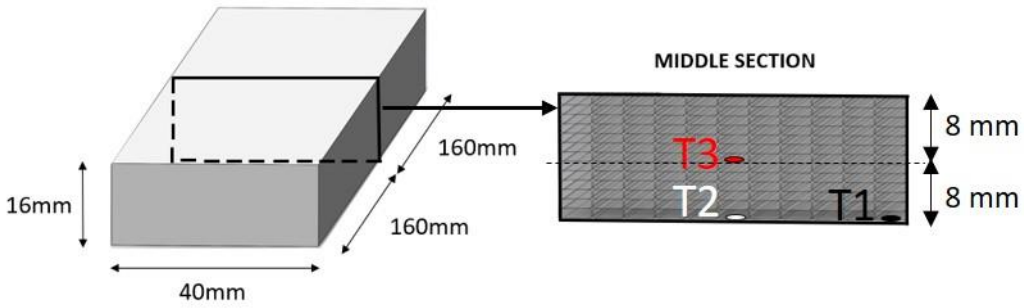

Fig. 3. Thermocouple locations in the middle cross section of the part.

2.4 Differential Scanning Calorimetry (DSC)

In order to study the thermal properties of PLA, Differential Scanning Calorimetry (DSC) analysis was performed with a DSC 1 (Mettler Toledo, Switzerland). Approximately 7 mg samples were cut

from the original parts or pellets and sealed in an aluminum pan. Nitrogen was fluxed to prevent polymer degradation. The degree of crystallinity χ_c of the samples was calculated as follows:

$$\chi_c = (\Delta H_m - \Delta H_{cc})/\Delta H_m^0 \quad (1)$$

where ΔH_m and ΔH_{cc} are the enthalpies of melting and cold crystallization, respectively, while ΔH_m^0 represents the melting enthalpy of a theoretical 100% crystalline PLA. This value was taken equal to 97.3 J/g, as used in the work of Bayart et al. (2021).

Two thermal protocols were applied on pellets to study dynamical (Protocol A) and isothermal (Protocol B) crystallization of PLA, as reported in Fig. 4a & b. Protocol A comprised a first heating performed from -40 to 250°C at 10°C/min aimed at removing thermal history. The sample was then cooled down from 250 to -40°C at various cooling rates V_{cool}, ranging between 0.5 and 20°C/min (in particular, V_{cool} = 0.5, 1, 2.5, 5, 10 and 20°C/min were chosen). Finally, the sample was re-heated from -40 to 250°C at 10°C/min to determine the degree of crystallinity that was reached after the different cooling steps.

Like for Protocol A, Protocol B initially consisted of a first heating performed from -40 to 250°C at 10°C/min to remove the thermal history. Then, the sample was quenched from 250°C to an isothermal temperature T_{iso} that was kept constant for 1 hour. Such a time interval was chosen based on the average time that was needed to 3D print the samples that were described previously, while T_{iso} ranged between 60 and 150°C with a 10°C increment. After the isothermal step, the sample was quenched from T_{iso} to -40°C and immediately re-heated from -40 to 250°C at 10°C/min to calculate its degree of crystallinity that was reached after the isothermal step.

Another thermal protocol (named Protocol C, Fig. 4c) was applied on compression molded and 3D printed samples to calculate the degree of crystallinity consequent to their manufacturing, thus Protocol C consisted only in a single heating performed from -40 to 250°C at 10°C/min.

The printed parts, built without the insertion of the thermocouples, were cut to extract small portions corresponding to the three virtual locations of the T1, T2 and T3 thermocouples. This allowed to correlate the evolution of bead temperature with the degree of crystallinity of the polymer at the three locations of interest in the printed part.

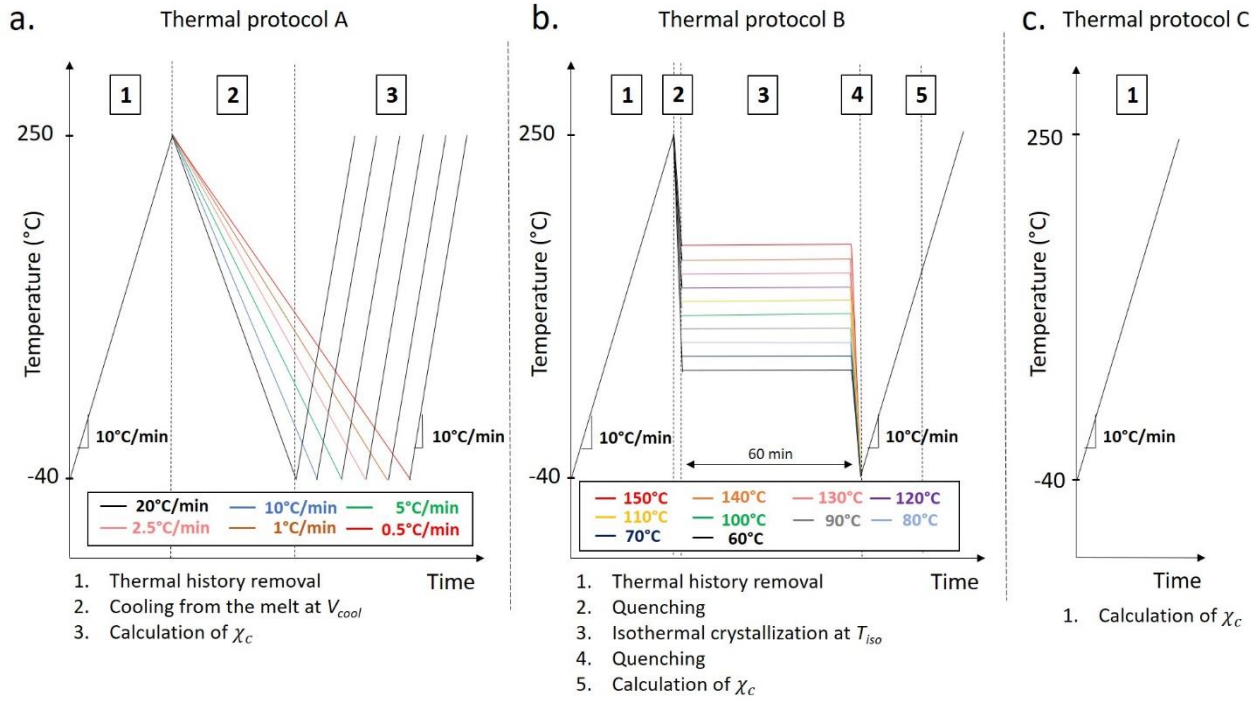

Fig. 4. Schematic representation of the two thermal protocols applied on pellets a) with different cooling rates (Protocol A), b) with different isothermal temperatures (Protocol B) and c) the thermal protocol applied on compression molded and 3D printed samples (Protocol C).

2.5 Bending tests

Three-point bending tests on all the parts obtained by 3D printing and compression molding were performed at room temperature at 2 mm/min cross head speed with a 10 kN load cell using a universal testing machine (Instron 1185, INSTRON, USA). Before testing, the parts were conditioned for 24 h at 21.5°C and 50% relative humidity. Because the dimensions of the 3D printed parts were four times higher than the compression molded ones, the span was also four

times higher (i.e., the span of the 3D printed parts and compression molded ones was fixed at 256 mm and 64 mm, respectively). A D5/400AG LVDT sensor (RDP Electronics) was used to measure the displacement at the middle cross section. Results were calculated from 3 reproductible tests.

3 RESULTS AND DISCUSSIONS

3.1 Dimensions of a unitary bead

Parts were printed with several bead volumes that had to be defined for each part. The bead volume (V) could be calculated using:

$$V = BS * L, \quad (2)$$

where *BS* is the transversal cross section (i.e., the transversal bead surface) and *L* the length of each bead. Since the length of each bead is identical for all samples, bead volume and bead surface differ by a constant scale factor.

An oblong geometry (Fig. 5) could be used to approximately describe the *BS*.

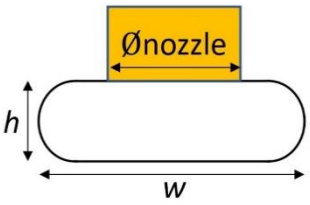

Fig. 5. Oblong geometry chosen to describe the transversal cross section of bead (*BS*).

From the oblong geometry, the *BS* can be quantified using the following equation:

$$BS = (w - h)\, h + \pi(h/2)^2 \ , \quad (3)$$

with *w* and *h* being the bead width and height, respectively, that was determined after printing. In fact, despite the superimposed bead width was chosen to be equal to the nozzle diameter (*N*)

multiplied by 1, 1.25, 1.75 and 2.5, a few variations between the experimental and the set bead width *w* could be noticed. The same can be said regarding the bead height *h*. The *BS* value for each printing condition is then reported in Tab. 2. It was convenient for the development of the article that all 3D printed parts be named with the code NX_BSYY.Y, with the X digit representing the nozzle diameter in mm that was used, while YY.Y is the BS area in mm^2.

Table 2. Measured geometric parameters for each printing conditions.

Sample	**Nozzle diameter (mm)**	**Set bead width (mm)**	**Measured bead width (mm)**	**Measured bead height (mm)**	**Estimated bead section (mm^2)**
N3_BS2.9	3	3	3.0 ± 0.04	1.05 ± 0.02	2.91
N3_BS4.4		3.75	3.8 ± 0.05	1.23 ± 0.02	4.35
N3_BS6.4		5.25	5.2 ± 0.06	1.31 ± 0.03	6.44
N3_BS10.4		7.5	7.5 ± 0.06	1.45 ± 0.03	10.42
N5_BS7.3	5	5	5.2 ± 0.05	1.50 ± 0.03	7.32
N5_BS9.1		6.25	6.4 ± 0.04	1.50 ± 0.04	9.12
N5_BS13.4		8.75	9.0 ± 0.06	1.55 ± 0.04	13.43
N5_BS29.1		12.5	12.4 ± 0.06	2.45 ± 0.06	29.09
N8_BS15.7	8	8	8.3 ± 0.05	2.00 ± 0.05	15.74
N8_BS20.1		10	10.5 ± 0.06	2.00 ± 0.05	20.14
N8_BS33.2		14	13.8 ± 0.07	2.50 ± 0.06	33.16
N8_BS60.2		20	19.5 ± 0.07	3.20 ± 0.07	60.20

Tab. 2 shows that the measured bead dimensions were relatively well controlled. As an example, the bead widths are in good agreement with the reference ones, as they differ by 0.5 mm at the most.

3.2 Thermal properties of PLA

A precise knowledge of the thermal behavior of PLA is important for understanding the physical phenomena that occur during a production run. In fact, during the production run, the temperature of the polymer decreased from the nozzle to room temperature following a complex thermal history and this in turn determined the microstructure of the final product.

In order to measure the basic thermal properties of the material, a common heating-cooling-heating thermal protocol was performed at 10°C/min on a PLA pellet to measure its glass transition (T_g) and melting (T_m) temperatures. From the second heating, the PLA pellets T_g was estimated at 60°C, while T_m was 172°C, in agreement with usual values for semicrystalline PLA.

During a production run, the PLA beads underwent a thermal history characterized by an initial fast cooling from the nozzle temperature, followed by intermittent re-warmings due to the subsequent deposition of other beads and layers, next to the considered one. At this stage the temperature showed little variations and thus it could be assumed uniform as a first approximation. After this phase, cooling proceeded down to room temperature.

In order to have a good idea of the PLA microstructure that was developed, especially in the first portion of the production run, Protocol A was used to study PLA crystallization at the various cooling rates V_{cool}. The results are pictured in Fig. 6a. As expected, crystallinity decreases as the cooling rate increases, reaching its maximum at about 57% for the slowest cooling rate (i.e., 0.5°C/min), while the material remains amorphous at cooling rates that are equal or higher than 10°C/min.

Protocol B, on the other hand, was used to estimate the ability of PLA to crystallize at different isothermal temperatures T_{iso}. The values of T_{iso} were chosen between 60 and 160°C with a 10°C increment. The results are pictured in Fig. 6b. As expected, if $T_{iso} \leq 80$°C and $T_{iso} \geq 150$°C, PLA is not able to crystallize and an appreciable degree of crystallinity is measured only when 90°C $\leq T_{iso} \leq$ 140°C, with its maximum at the midpoint of such a range, i.e., around T_{iso} = 120 – 130°C. The results are in line with those pictured in Fig. 6a relative to the effects of the cooling rate in terms of the highest obtainable crystallinity (i.e., χ_c = 58%).

Summing everything up, the material is able to crystallize only if the cooling rate is lower than 10°C/min and if the constant temperature is between 90 and 140°C for a sufficient period of time. In all other thermal conditions PLA does not crystallize and remains amorphous.

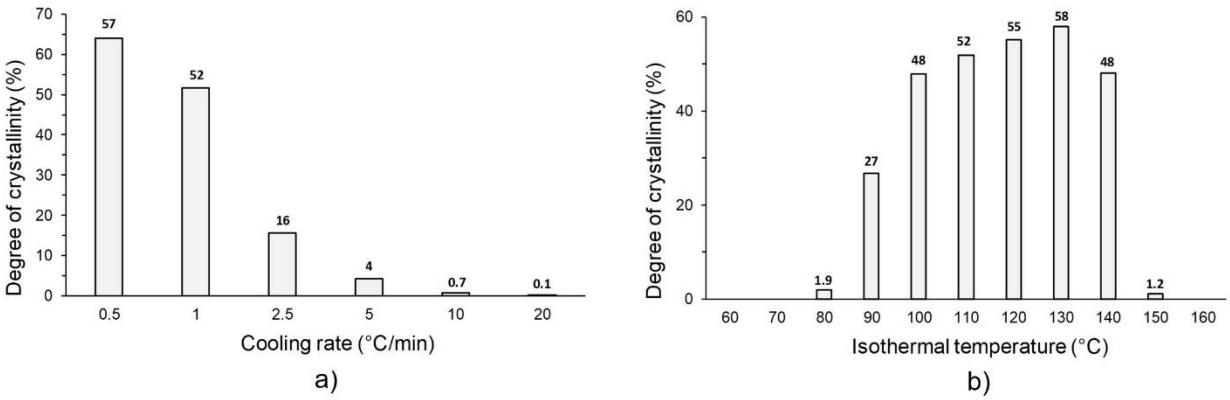

Fig. 6. Degree of crystallinity determined from pellets using (a) Protocol A and (b) Protocol B.

3.3 Thermal history of 3D printed parts

Once the PLA thermal behavior is known, the thermal history as a function of time can be considered at the three locations of interest (i.e., T1, T2 and T3). For illustrating purposes, only four printing conditions are reported in Fig. 7. These were chosen as the smallest *BS* made with the 3 mm nozzle (Fig. 7a), the largest ones printed with the 8 mm nozzle (Fig. 7d) and those corresponding to the central *BS* obtained through the 5 mm nozzle (Figs. 7b and 7c).

In general, it is evident that, on average, the measured temperature at T1 is lower than that at location T2, which in turn is lower than T3. This can be easily explained, as T1 was on the upper surface of the first bead, close to the edge. For these reasons, it had a faster cooling rate and hence an average temperature that was lower than the other locations. The T2 location was in the middle of the section but in the bottom, thus in contact with the build plate that in the present case was not heated. The T3 location was in the center of the section, thus it was surrounded by the polymeric material that is a good thermal insulator.

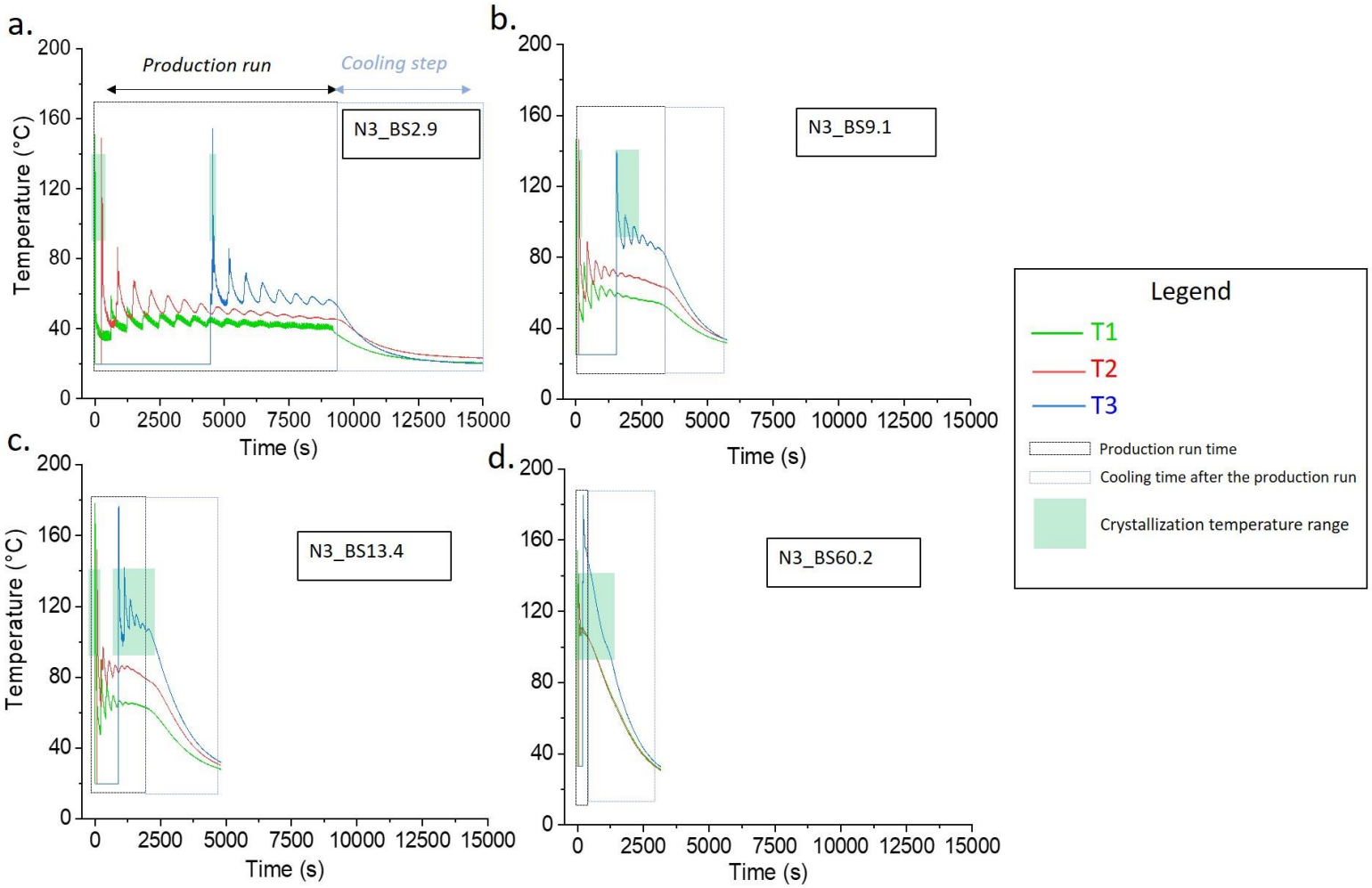

Fig. 7. Whole thermal histories at the 3 locations T1, T2, T3 during the production run until cooling down for (a) N3_BS2.9; (b) N5_BS9.1; (c) N5_BS13.4; (d) N8_BS60.2.

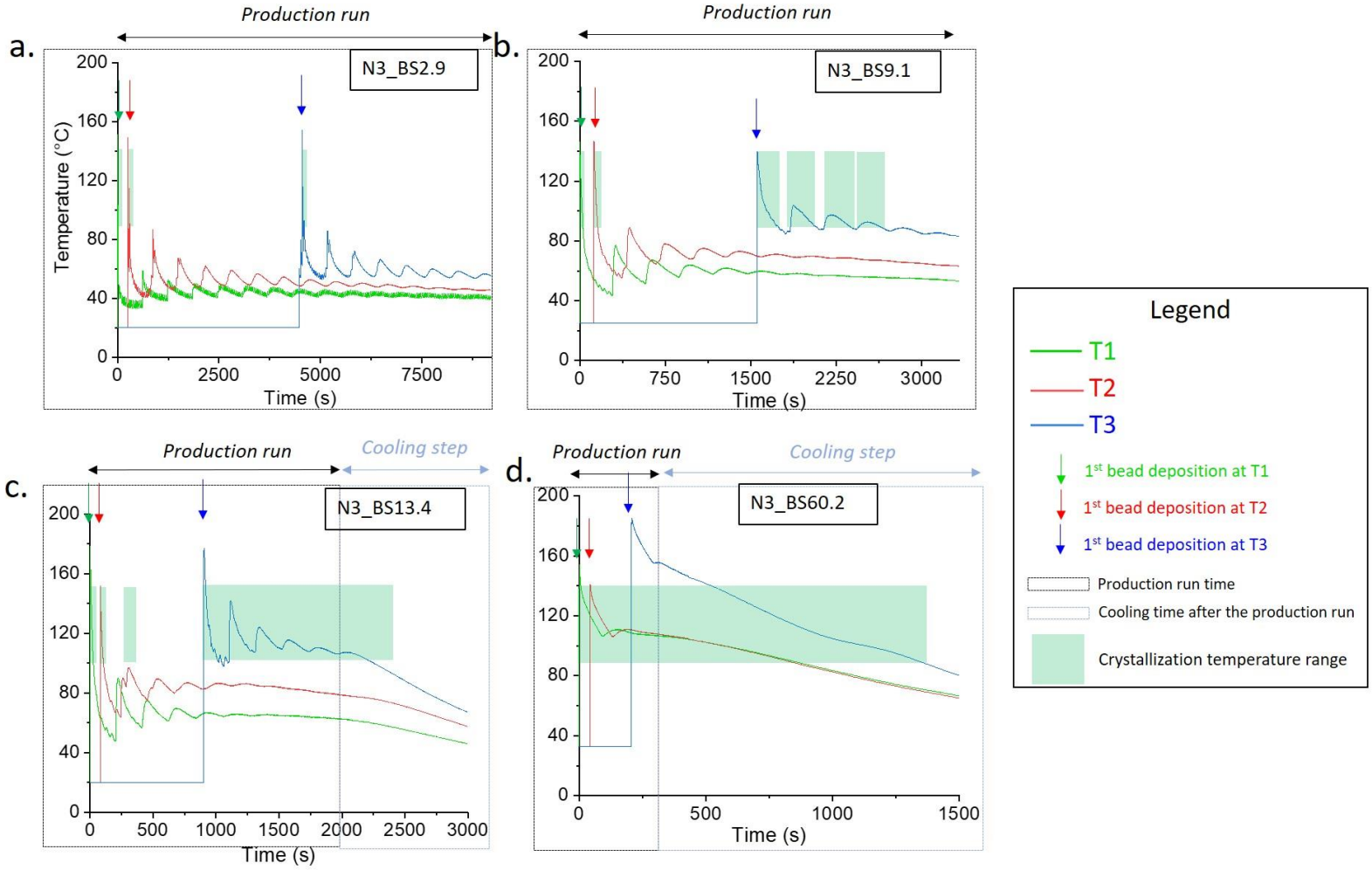

Fig. 8. Zoom of subfigures in Fig.7. showing the ability of the polymer to crystallize as function of the 3 locations T1, T2, T3 during the production run until cooling down for (a) N3_BS2.9; (b) N5_BS9.1; (c) N5_BS13.4; (d) N8_BS60.2.

With the exception of the largest BS, the thermal histories consisted of a cooling from the melt with a series of successive reheating steps, which were due to the deposition of material during the production run and nozzle thermal radiation, followed by a final cooling down to room temperature once the production run was finished. For all *BS*, the first peak starts at the highest temperature, close to the nozzle temperature. The subsequent ones are due to the deposition of beads constituting layers above the considered location. These peaks show a relevant attenuation because at each successive peak the distance between the thermocouple and the subsequently deposed beads increases. Moreover, the time interval between these peaks decreases as the *BS* becomes larger, because the print time of a single layer becomes smaller (e.g., the time to print a layer made of small 15 beads (N3_BS2.9) was much higher than the one to print a layer made of 2 big beads (N8_60.2)).

In Figs. 7a and 7b small amplitude and high frequency peaks are also visible, especially at the T1 location. These are due to the deposition of beads within the same layer next or close to the considered one. Indeed, their frequency is equal to $2.4.10^{-2}$ Hz, which corresponds to the 41 s time between two successive bead deposition. The reason for the higher visibility of these peaks at the T1 location of Figs. 7a and 7b is due to the smaller thermal inertia of small beads and to the faster cooling of this location with respect to the other ones, as it is closer to the exterior boundary.

The temperature range at which crystallization occurs is highlighted in green, and this is important to understand the crystallinity measurements that will be presented and discussed next. Notice, though, that to understand the crystallinity results properly, it must be clear that not only temperature shall be considered, but also the permanence time within the crystallization range. As larger BS possess higher thermal inertia, the average temperature in the parts increases with BS and the cooling of the single beads requires more time as well. Understandably, this has a clear consequence on crystallization ability. On the other hand, at smaller *BS* the number of deposed

beads is higher, and this induces more re-heating steps, which keep the average temperature for a longer time within crystallization range, especially in the center of the part, i.e., at T3 (see Figs. 7b & 7c). As a result, crystallization is not easy to predict, and the precise quantification presented next helps understanding this phenomenon better.

3.4 Degree of crystallinity of the PLA in 3D printed and compression molded samples

The degrees of crystallinity χ_c at the various locations of interest, T1, T2 and T3, were measured for each *BS* using Protocol C and are displayed in Fig. 8.

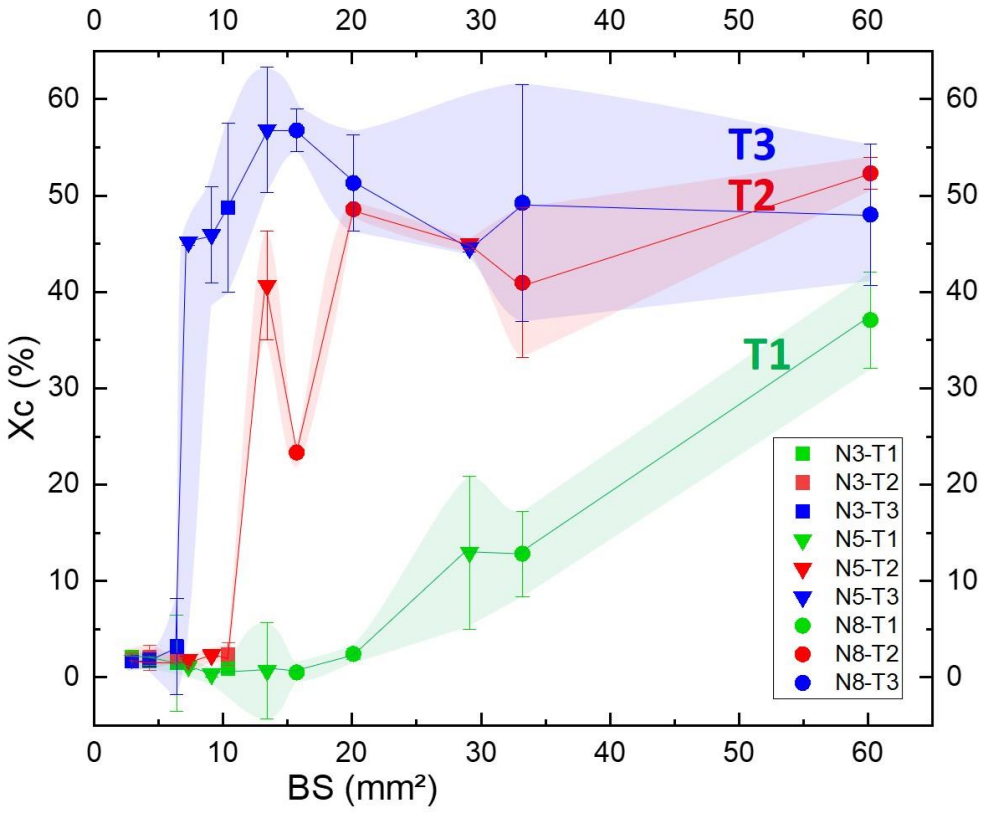

Fig. 8. Degree of crystallinity of 3D printed parts at locations T1, T2, T3 measured through thermal protocol C.

Crystallinity at T1 is always lower than at other locations for all BS, except perhaps in the largest section (i.e. 60.2 mm^2). This is a direct consequence of the cooling rate at this location, which is quite high except for the highest BS, as evident from Fig. 7, and low crystallinity is induced as a result of Fig. 6a. A precise gradual increasing trend of crystallinity as a function of BS is clearly visible for the T1 location. Interestingly, this is independent of nozzle diameter, in that the experimental points fall on this trend for all nozzles that were used. It can be deduced that the main reason for this behavior is the thermal inertia of the deposed bead, which is independent of the nozzle: a larger bead would simply cool down more slowly than a smaller one, determining a higher crystallinity.

A certain trend that is independent of the nozzle diameter can be recognized also for the T2 and T3 locations, but it differs a lot from that of T1. In particular, for both locations a BS threshold can be identified, at which crystallinity increases sharply, going from a basically amorphous material to a crystallinity above 40%. This threshold is about 14 mm^2 for the T2 location and 7.5 mm^2 for the T3 location. After the threshold, a maximum is reached, then crystallinity almost levels up to a plateau value, slightly below the maximum.

The higher crystallinity at the T2 and T3 locations is due to the surrounding beads that are laid around the locations of interest, which determine a lower cooling rate and a continuous reheating. In particular, both T2 and T3 were far from the part edge and T3 was completely surrounded by the other deposed beads, thus it was deposed over a warm surface and was kept for a longer time at a temperature where crystallization could occur. The result is slower cooling rates and longer periods of time close to the crystallization temperature range. From Fig. 7, this is evident for T3 at all BS except the smallest one, and for T2 in Fig. 7c and 7d.

DSC crystallinity readings are confirmed also by visual inspection of the part cross sections, as reported in Fig. 9 and listed in ascending order of BS. A translucid, almost transparent, appearance

can be associated to an amorphous material while opaque portions indicate the presence of crystallization. It can be seen that the more crystalline material is located in the central part of the section, while the amorphous material is mostly located at the boundaries, in agreement with Fig. 7. Moreover, at greater *BS* the crystalline portion increases its size, e.g., with a *BS* that is less than 4.3 mm^2 the part is in a mainly amorphous state, while starting from a *BS* of 6.4 mm^2 the crystalline zone is present in the center and reaches the lateral edges at $BS \geq 13.4$ mm^2. At $BS > 60.2$ mm^2, the part becomes completely semi-crystalline.

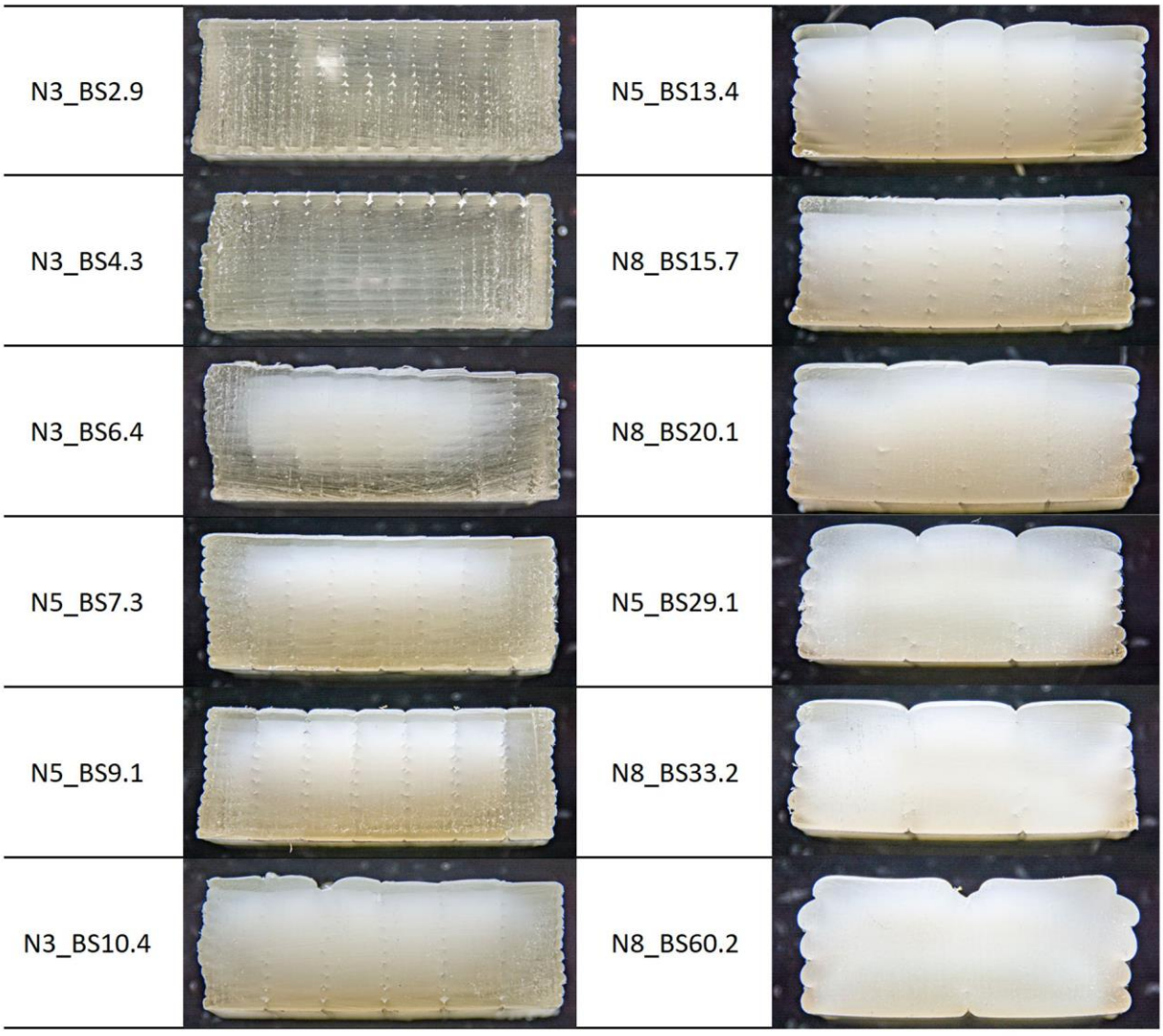

Fig. 9. Transversal cross sections of the 3D printed parts for each set *BS*

For completeness and for better explaining the mechanical properties that are presented next, also crystallinity of compression molded part was measured through Protocol C. In particular, the part that was quenched presented a 3% degree of crystallinity, thus virtually completely amorphous as expected, while the part that was slowly cooled after compression molding was 55% crystalline.

3.5 Bending tests

In Fig. 10, typical stress vs. strain curves for the same parts of Fig. 7 are reported. Two different mechanical behaviors can be recognized. In one case, the material is stiffer but less strong and more brittle with strain at break below 2% and characterized by a completely linear elastic behavior; in the other case the material is stronger, less stiff and has a strain at break greater than 2%, displaying also some yielding behavior, identified as a slight deviation from linearity of the stress strain curve.

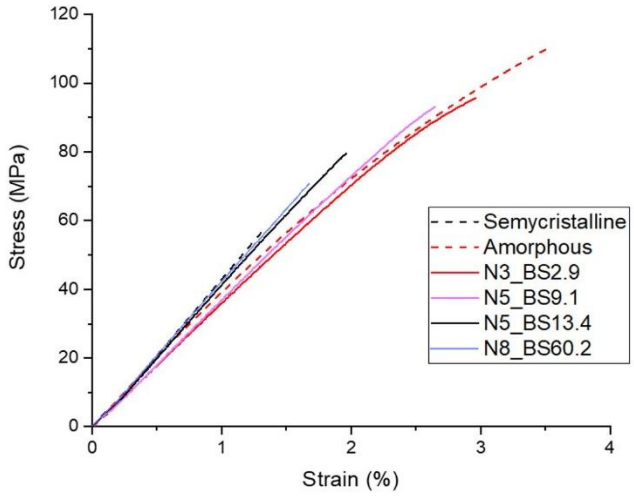

Fig. 10. Stress vs strain curves for compression molded parts and a selection of 3D printed parts

Quenched compression molded parts together with parts that were 3D printed with small *BS* (i.e., the predominantly amorphous materials) belong to this last group, while the slowly cooled compression molded ones and those printed with larger *BS* (i.e., the more crystalline parts) are part

of the former one. Interestingly, parts printed through the 5 mm nozzle may belong to any of the two groups, depending on their BS.

From a quantitative point of view, the complete results in terms of Young's modulus, ultimate stress and strain at break for all 3D printed and compression molded parts are reported in Fig. 11. In general, the standard deviation of all measurements is quite small, thus denoting a good repeatability within the printing conditions. Concerning the compression molded parts, their Young's moduli are about 3500 MPa for the quenched PLA and about 4500 MPa for the slowly cooled one. There is thus a difference of 1 GPa, or about 25%, and this may be well explained by the difference in crystallinity. On the other hand, the strain at break of the amorphous material is about three times as much that of the semi-crystalline one (3.8% vs. 1.3%), and this higher toughness induces an almost double strength value (107 MPa vs. 59 MPa). This behavior was already observed by Perego et al. (1996) and is not unexpected, since it can be explained on the basis of crystallite size that are present in the material, in that large crystals lead to a more brittle behavior (Razavi and Wang, 2019): the low strain at break comes from the crack propagating preferentially through the large interfaces between the amorphous and the crystalline phases. It was shown by Yang et al. (2011) that either a slow cooling from the melt or an annealing at relatively high temperature promote a high crystallite growth rate of PLA, thus leading to large spherulites. This is precisely what happens during the preparation of the slowly cooled compression molded specimens. If a tougher behavior was to be obtained, crystal nucleation rate should be enhanced over crystal growth rate, thus it would be beneficial either to quench the material and then anneal it at a temperature that is lower than 100°C (Yang et al. 2011), or use a suitable nucleating agent, e.g., pectin (Satsum et al., 2022).

Concerning the 3D printed parts, all mechanical properties are completely included within the interval that is determined by the compression molded parts. It can be seen that the most important parameter that describes the behavior is anyway the *BS*, in fact the mechanical properties display a

typical trend as a function of the *BS*, and this occurs independently of the specific nozzle that was used, similarly as what was observed for crystallinity.

In fact, the Young's modulus shows a *BS* threshold between 10.4 and 13.4 mm^2 (Fig. 11a), which is perfectly in line with the crystallinity threshold value relative to location T2 in Fig. 8: below such a threshold the material is more compliant and behaves similarly to the amorphous compression molded parts, above this threshold the material is stiffer and shows Young's moduli that are close to that of the slowly cooled compression molded parts. Within each group there are only little differences among the various printing conditions, while across the threshold the difference is definitely larger.

The reason for the agreement between stiffness results and crystallinity at T2 is most probably related to the type of loading, i.e., bending: in this case the material carries most of the applied load in the upper and lower portions of the cross section (far from the neutral plane), and this region is indeed best represented by T2 among the three locations that were selected.

The same behavior can be found also in the strain at break histogram of Fig. 11b, where the same threshold can be recognized, this time identifying a transition from a relatively large ultimate strain (i.e. in excess of 2%) to a smaller one. Semi-crystalline compression molded parts have indeed a very low strain at break, slightly above 1%, making this material particularly brittle.

The behavior in terms of ultimate stress (Fig. 11c) is more difficult to explain. Again, the behavior seems to respect the threshold that was identified previously, but the difference between the two groups is less evident than in Fig 11a and b. Predominantly amorphous 3D printed materials possess strength values that are quite high and uniform, being in the 85 – 95 MPa range, but none of them comes close to the almost 110 MPa strength displayed by the amorphous compression molded parts. The semi-crystalline parts, on the other hand, display lower strength values and have a decreasing trend with the *BS*, going from 83 MPa down to 68 MPa, thus almost reaching the strength of the

slowly cooled compression molded material at 59 MPa. In any case it is worth remarking that the bending tests results are in good agreement with the degree of crystallinity results that were described in the previous section.

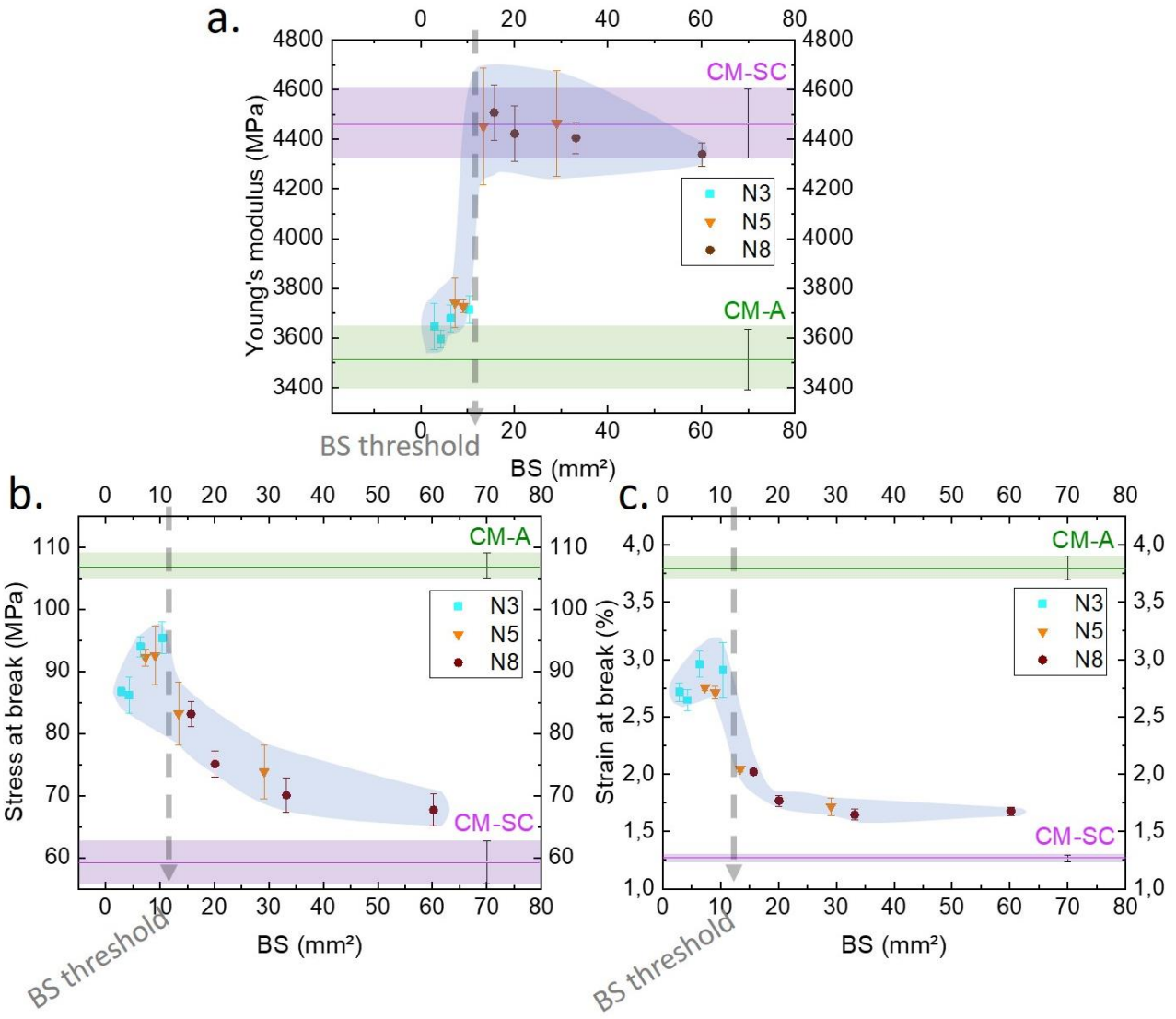

Fig. 11. Mechanical properties for compression molded and 3D printed parts at different *BS*. (a) Young's modulus; (b) Stress at break; (c) strain at break.

4. Conclusions

In this paper, the mechanical and thermal properties of parts made of a semicrystalline PLA fabricated by a large-scale material extrusion 3D printer were studied concerning their relationship

with geometric quantities such as the bead volume. It was found that this parameter has a profound influence on the degree of crystallinity, as a result of the differences in average temperature and permanence time at the temperature range, at which crystallization can occur. Such differences in crystallinity have a direct consequence on the mechanical properties. In particular, the more crystalline material appears to be stiffer but also more brittle and weaker. A variation of bead width from 3 to 20 mm was found to be at the origin of an increase in the PLA degree of crystallinity from 0 to almost 50% causing an increase in the Young's modulus of the resulting material from 3.6 GPa to 4.3 GPa and a decrease in the strain at break from 3 to 1.7%

These results can be explained by the different thermal histories measured precisely at three different locations for each part type. These conditions, in fact, depend not only on the bead volume but also on the various parameters that influence the heat transfer between the deposed polymer and the surrounding environment. This in turn gives rise to crystallinity inhomogeneities within the part cross section, and consequently affects the resulting mechanical properties.

From a fundamental point of view, the paper highlights the link between the degree of crystallinity generated during manufacturing and the mechanical properties of 3D printed parts. This proves the highly significant effects of processing conditions on material mechanical behavior, which is typical of traditional polymer processing techniques but is met also in material extrusion 3D printing. The bead volume must then be carefully chosen, in such a way that the mechanical properties of large 3D printed parts are suitable for the selected application. On the basis of this research, a more specific study is ongoing to describe the evolution of polymer crystallinity as a function of time under the real thermal history undergone by the beads at the three locations of interest. The results will be published elsewhere in the incoming future.

Acknowledgements

The authors are deeply grateful to Mr. Mirko Viviani for assistantship with the picture of Fig. 11.

References

Alsoufi et al. (2017) Alsoufi, M.S., El-Sayed A., 2017. Warping Deformation of Desktop 3D Printed Parts Manufactured by Open Source Fused Deposition Modeling (FDM) System, Int. J. Mech. Mechatron. Eng. 17, 7-16.

Bayart et al. (2021) Bayart, M., Foruzanmehr, M.R., Vuillaume, P.Y., Ovlaque, P., Robert, M., Elkoun, S., 2021. Poly(lactic acid)/flax composites: effect of surface modification and thermal treatment on interfacial adhesion, crystallization, microstructure, and mechanical properties, Compos. Interfaces, 29, 17-36.
https://doi.org/10.1080/09276440.2021.1884470.

Behzadnasab et al. (2016) Behzadnasab, M., Yousefi, A.A., 2016. Effects of 3D printer nozzle head temperature on the physical and mechanical properties of PLA based product, 12th International seminar on polymer science and technology, 3-5.

Cleeman et al. (2022) Cleeman, J., Bogut A., Mangrolia B., Ripberger A., Kate K., Zou Q., Malhotra R., 2022. Scalable, flexible and resilient parallelization of fused filament fabrication: Breaking endemic tradeoffs in material extrusion additive manufacturing, Addit. Manuf. 56, 102926 https://doi.org/10.1016/j.addma.2022.102926

Costa al al. (2017) Costa, S.F., Duarte, F.M., Covas, J.A., 2017. Estimation of the filament temperature and adhesion development in fused deposition techniques, J. Mater. Process. Technol., 245, 167-179.
https://doi.org/10.1016/j.jmatprotec.2017.02.026

Dorez et al. (2019) Dorez, Y., Lacrampe, M.F., Soulestin, J., 2019. Improved Tool for Depositing Material in Three Dimensions by Extrusion, International patent, WO 2019/141946.
https://patents.google.com/patent/WO2019141946A1/fr.

Forster et al. (2015) Forster, A.M., 2015. Materials Testing Standards for Additive Manufacturing of Polymer Materials: State of the Art and Standards Applicability, NISTIR 8059.
https://doi.org/10.6028/NIST.IR.8059.

Gupta et al. (2021) Gupta, A.K. Taufik, M., 2021. Effect of process variables on performances measured in filament and pellet based extrusion process, Mater. Today. 47, 5177-5184.
https://doi.org/10.1016/j.matpr.2021.05.508.

Habeeb et al. (2016) Habeeb, H.A., Alkahari, M.R., Ramli, F.R., Hasan, R., Maidin, S., 2016. Strength and porosity of additively manufactured PLA using a low cost 3D printing, Conference: Mechanical Engineering Research Day. 69-70.

Jin et al. (2017) Jin, Y.J., Wan. Y., Zhang, B., Liu, Z., 2017. Modeling of chemical finishing process for polylactic acid parts in fused deposition modeling and investigation of its tensile properties, J. Matter. Process. Technol. 240, 233-239.
https://doi.org/10.1016/j.jmatprotec.2016.10.003

Kristiawan et al. (2021) Kristiawan, R.B., Imaduddin, F., Ariawan, D., Ubaidillah., Arafin Z., 2021. A review on the fused deposition modeling (FDM) 3D printing: Filament processing, materials, and printing parameters, Open Eng. 11, 639–649.
https://doi.org/10.1515/eng-2021-0063.

Kuznetsov et al. (2018) Kuznetsov, V.E., Solonin, A.N., Urzhumtsev, O.D., Schilling, R., Tavitov, A.G., 2018. Strength of PLA Components Fabricated with Fused Deposition Technology Using a Desktop 3D Printer as a Function of Geometrical Parameters of the Process, Polymers. 10, 313.
https://doi.org/10.3390/polym10030313.

Li et al. (2018) Li, H., Wang, T., Sun, J., Yu, Z., 2018. The effect of process parameters in fused deposition modelling on bonding degree and mechanical properties, Rapid Prototyp. J. 24, 80-92.
https://doi.org/10.1108/RPJ-06-2016-0090.

Lia et al. (2019) Liao, Y., Liu, C., Coppola, B., Barra, G., Di Maio, L. Incarnato, L., Lafdi, K., 2019. Effect of Porosity and Crystallinity on 3D Printed PLA Properties, Polymer. 11, 1487.
https://doi.org/10.3390/polym11091487.

Mazzanti et al. (2019) Mazzanti, V., Malagutti, L., Mollica, F., 2019. FDM 3D Printing of Polymers Containing Natural Fillers: A Review of their Mechanical Properties, Polymers. 11, 1094.
https://doi.org/10.3390/polym11071094.

Malagutti et al. (2022a) Malagutti, L., Ronconi, G., Zanelli, M., Mollica, F., Mazzanti, V. 2022. A post-processing method for improving the mechanical properties of Fused-Filament-Fabricated 3D-printed parts, Processes 10, 2399.
https://doi.org/10.3390/pr10112399

Malagutti et al. (2022b) Malagutti, L., Mazzanti, V., Mollica, F., 2022. Tensile properties of FDM 3D printed wood flour filled polymers and mathematical modeling through classical lamination theory, Rapid Prototyp. J. 9, 1834-1842.
https://doi.org/10.1108/RPJ-11-2021-0298

NorthcuttSara (2018) NorthcuttSara, L.A., OrskiKalman, V., Migler, B., Kotula, A.P., 2018. Effect of processing conditions on crystallization kinetics during materials extrusion additive manufacturing, Polymer. 154, 182-187.
https://doi.org/10.1016/j.polymer.2018.09.018.

Perego et al. (1996) Perego, G., Cella, G.D., Bastioli, C., 1996. Effect of Molecular Weight and Crystallinity on Poly(lactic acid) Mechanical Properties, J. Appl. Polym. Sci. 59, 37-43.
https://doi.org/10.1002/(SICI)1097-4628(19960103)59:1<37::AID-APP6>3.0.CO;2-N.

Razavi and Wang (2019) Razavi, M., Wang, S.Q., 2019. Why is crystalline poly(lactic acid) brittle at room temperature? Macromolecules 52, 5429 – 5441.

Satsum et al. (2022) Satsum, A., Busayaporn, W., Rungswang, W., Soontaranon, S., Thumanu, K., Wanapu, C. 2022. Structural and mechanical properties of biodegradable poly(lactic acid) and pectin composites: using bionucleating agent to improve crystallization behavior, Polymer J. 54, 921 – 930.

https://doi.org/10.1038/s41428-022-00637-9

Shail el al. (2021) Shaik, Y.P., Schuster, J., Shaik, A., 2021. A Scientific Review on Various Pellet Extruders Used In 3D Printing FDM Processes, Open Access Libr. 8, 1-19.
https://doi.org/10.4236/oalib.1107698.

Sooda et al. (2010) Sooda, A.K., Ohdarb, R.K., Mahapatrac, S.S., 2010. Parametric appraisal of mechanical property of fused deposition modelling processed parts, Mater. Des. 31, 287-295.
https://doi.org/10.1016/j.matdes.2009.06.016.

Vadori et al. (2013) Vadori, R., Mohanty, A.K., Misra, M., 2013. The Effect of Mold Temperature on the Performance of Injection Molded Poly(lactic acid)-Based Bioplastic, Macromol. Mater. Eng. 298, 981–990.
https://doi.org/10.1002/mame.201200274.

Wang et al. (2017) Wang, L., Gramlich, W.M., Gardner, D.J., 2017. Improving the impact strength of Poly(lactic acid) (PLA) in fused layer modeling (FLM), Polymer. 114, 242- 248.
http://dx.doi.org/10.1016/j.polymer.2017.03.011.

Wasanasuk et al. (2011) Wasanasuk, K., Tashiro, K., 2011. Crystal structure and disorder in Poly(L-lactic acid) d form (a0 form) and the phase transition mechanism to the ordered a form, Polymer. 52, 6097-6109.
https://doi.org/10.1016/j.polymer.2011.10.046.

Yang et al. (2011) Yang, G., Su, J., Su, R., Zhang, Q., Fu, Q., Na, B., 2011. Toughening of poly(l-lactic acid) by annealing: the effect of crystal morphologies and modifications, J. Macromol. Sci. B: Physics, 51, 184 – 196.
https://doi.org/10.1080/00222348.2011.565263

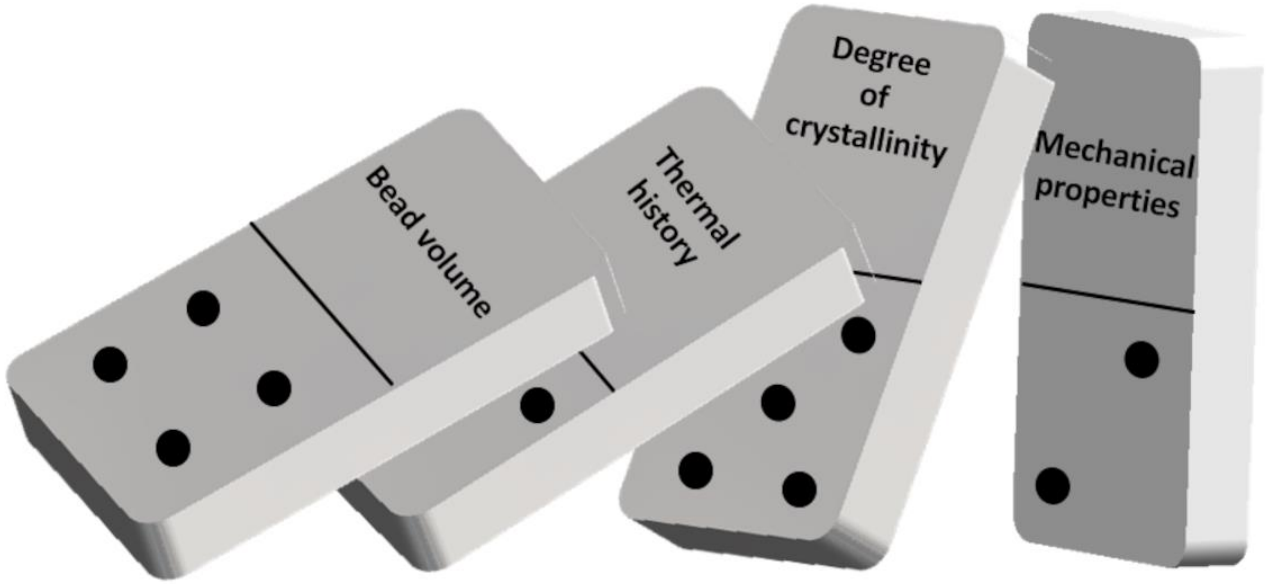
Bead volume
Thermal history
Degree of crystallinity
Mechanical properties

GA